Heliyon 9 (2023) e16107

Contents lists available at ScienceDirect

Heliyon

journal homepage: www.cell.com/heliyon

Research article

Service life assessment of yttria stabilized zirconia (YSZ) based thermal barrier coating through wear behaviour

Pushpak Banerjee [a], Avinava Roy [a], Soumyadeep Sen [a], Arkajit Ghosh [a], Gourab Saha [b], Asiful H. Seikh [c], Ibrahim A. Alnaser [c], Manojit Ghosh [a,*]

[a] Indian Institute of Engineering Science and Technology, Howrah, WB 711103, India
[b] Tampere University, Kalevantie 4, 33100 Tampere, Finland
[c] Mechanical Engineering Department, College of Engineering, King Saud University, Riyadh 11421, Saudi Arabia

ARTICLE INFO

Keywords:
Yttria-stabilized zirconia
Thermal barrier coatings
Microstructure
Wear
Coating durability

ABSTRACT

Countless research has suggested Yttria-stabilized Zirconia (YSZ) to be a top candidate for being implemented as thermal barrier coatings (TBC). However, when exposed to prolonged service, temperature and stress variations succeed in initiating a catastrophic phase transformation from tetragonal to monoclinic structure in Zirconia. Hence, the estimation of endurance for YSZ-based TBC is necessary to minimize failure in such situations. The main purpose of this research was to determine the relationship between tribological investigations and the estimated lifespan of YSZ coatings accurately. The study used various methods such as wear resistance testing, optical profilometry, specific wear rate, and coefficient of friction to estimate the maximum durability of TBCs. The research also provided insights into the composition and microstructure of the TBC system and found the optimized concentration of Yttrium doping to be 3.5 wt %. The study discovered that erosion was the main cause of roughness depreciation from SN to S1000. The estimation of the service life was primarily made based on optical profilometry, specific wear rate (SWR), coefficient of friction (COF) and wear resistance values which were further supported by the results of chemical characterization of the samples through electron dispersive spectroscopy (EDS), wavelength dispersive spectroscopy (WDS) and X-Ray Diffraction (XRD) analysis. The results were reliable and accurate and suggested future areas of investigation, such as 3D profilometry for surface roughness and thermal conductivity evaluation using laser-assisted infrared thermometers.

1. Introduction

Superalloys can be regarded as one of the most groundbreaking innovations in the domain of metallurgical applications, owing to their superior ability to perform appreciably at elevated temperatures. However, every application at high temperature encounters several drawbacks that threaten the durability of the superalloy. Thermal Barrier Coating (TBC) has served as a primary source of providing perturbatioin to. These coatings are used in various industrial applications, especially in environments experiencing surface attacks at elevated temperatures, like turbines [1], combustion chambers, blades, and vanes. Primarily based on ceramics, these TBCs combine the thermal resistance of ceramic coatings (surface) with the strength of superalloys (bulk), making them an ideal candidate

* Corresponding author.
E-mail address: mghosh.metal@faculty.iiests.ac.in (M. Ghosh).

https://doi.org/10.1016/j.heliyon.2023.e16107
Received 26 December 2022; Received in revised form 2 May 2023; Accepted 5 May 2023
Available online 6 May 2023

for high-temperature applications. The conventional TBC system consists of the bond coat (BC), which plays the role of primary resistance to oxygen, and a top coat (TC) made up of the ceramic layer and the base metal alloy (BA). Thermal insulation and corrosion resistance are the essential demands catered by this TC. At the same time, the BC also plays a crucial role in providing adhesion of the ceramic layer to the metal substrate [2]. These distinct layers have been succinctly represented in Fig. 1(a).

In terms of main fabrication methods, the preparation process can be subdivided based on multiple versions of thermal spraying techniques – vapour deposition (VD) and plasma spray (PS), among which the plasma-sprayed coating is the most popular. Thermal spray depends on numerous tractable and intractable factors and thus must be monitored closely to achieve a regular industry-ready coating [4]. Even the smallest altercations in the plasma cloud might lead to fatal problems, owing to its strong influence on the microstructure of the coating produced [5]. In the plasma cloud, the molten and solid particles move at a constant high velocity and collide with the substrate. As a result of these collisions, the particles are flattened out, nearly squashed and fused, forming the coating as we know it [6]. These flattened-out splats are separated by the interlamellar pores resulting from the rapid solidification giving rise to voids and cracks around unmelted particles by virtue of thermal stresses. These cracks and pores provide discontinuities in the pathway for unhindered heat flow. This, in turn, lowers the thermal conductivity of TBCs fabricated through the plasma spraying process.

PS can be broadly divided into vacuum plasma spray (VPS) and atmospheric plasma spray (APS) techniques. The extreme plasma temperatures operate at nearly 15,000 K, causing a high degree of particle melting, so even refractory materials such as oxides are not spared. APS is a highly preferred methodology as it produces a thermal load-bearing topcoat and high oxidation resistance at a comparatively lower cost.

Among the TBCs, Yttria stabilized Zirconia (YSZ) has emerged as one of the widely used composites owing to their excellent thermal shock resistance coupled with minimal thermal conductivity and high thermal expansion coefficient [7]. Understandably, the need for the low thermal conductivity of a TBC can be reasoned with the need for primary resistance to heat flow from the coating to the substrate underneath. The thermal conductivity of YSZ at high temperatures was most extensively measured by Kingery et al. [8], where the temperature was chosen as the parameter deciding the conductivity of multiple oxides. A temperature-independent conductivity at elevated temperatures (within the range of application for TBCs) has been reported. This phenomenon is very different from the 1/T correlation (as dictated by the Umklapp inelastic phonon-phonon scattering phenomenon [9]) between thermal conductivity and temperature for most other crystalline oxides – Fig. 1(a). The independence of temperature and conductivity in the case of YSZ can be correlated to the presence of many point defects that cause the scattering of phonons.

In order to prevent cracks generated by thermal stresses, a TBC with a value of the thermal expansion coefficient close to its substrate alloy is a crucial requirement. Even a tiny deviation or mismatch in the expansion coefficients between the coating layers (TC, BC, BA) might generate severe cracks under interlayer mechanical stresses [10]. To mitigate the thermal stresses, TBCs are designed to have a thermal expansion coefficient of similar magnitude of the substrate expansion value [11]. This comparable value of coefficient of thermal expansion helps to reduce the amount of stress that is transferred to the substrate during thermal cycling. For example, if a TBC has a thermal expansion coefficient that is too high, then the coating will expand more than the substrate during heating, and this will create tensile stresses at the interface between the TBC and the substrate [12,13]. These tensile stresses can cause cracking and spalling of the TBC, and it can also lead to the detachment of the coating from the substrate. In the case of pure Zirconia, the temperature fluctuations might initiate a phase transformation from its conventional cubic crystal structure. Various pieces of literature support the transformation of Zirconia from cubic structure to that of tetragonal, which being a metastable phase, further transforms to monoclinic structure [14,3]. This phase transformation accompanies a finite volume change of 4%, which contributes to the disintegration of the polycrystalline structure of Zirconia, resulting in a decrease in strength. In order to avoid this phenomenon, the use of ZrO_2 is often stabilized by divalent or trivalent additives such as Y_2O_3. This led to the emergence of YSZ as a potential candidate for topcoat material [13]. Moreover, a relatively lower valence of the Yttrium (Y) ions, compared to Zirconium (Zr) increases the oxygen

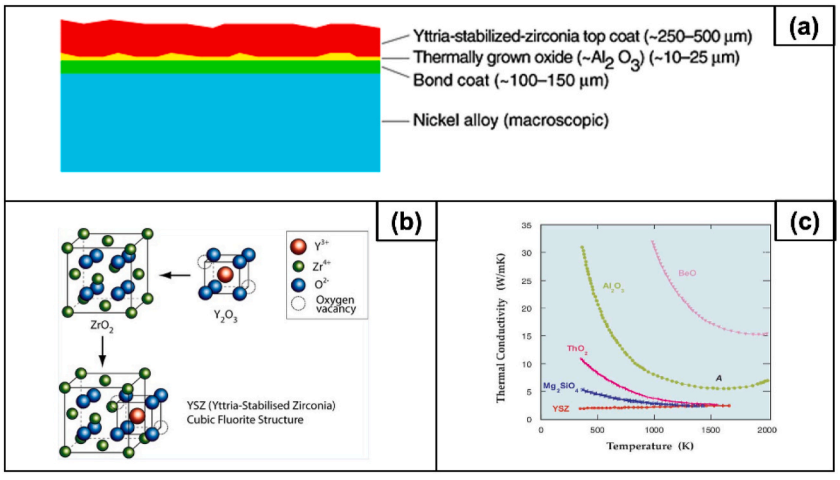

Fig. 1. (a) Schematic of a TBC (b) Stabilisation of Zirconia (c) Thermal conductivity vs temperature plots for refractory oxides [3].

vacancy leading to phonon scattering, which lowers thermal conductivity [15]. In terms of thermal expansion coefficient, YSZ offers an appreciably high value of expansion [16], along with high melting point, establishing its high suitability as a TBC.

Nevertheless, there is still a drawback associated with YSZ at higher operating temperatures. The metastable tetragonal phase under mechanical loads transforms into a cubic and another tetragonal phase. This newly formed tetragonal phase on cooling transforms again to a monoclinic structure, which is the primary room temperature phase for pure Zirconia as is depicted in Fig. 1(b). Subsequently, the accompanying volume change and stress developed in this process lead to cracking. Hence, the key to increasing fracture toughness is the stability or retention of the tetragonal phase with the help of stabilizers. Thus, it can be concluded that using a controlled amount of Yttrium as a doping agent plays a crucial role. The concentration of the Yttria is highly dependent on the severity of working conditions. For instance, 3 M-percents (n/n%) YSZ, alternatively known as Tetragonal Zirconia Polycrystals (TZP) exhibited relatively higher fracture toughness than (2, 6, 8, 12) n/n% of YSZ since 3 n/n% had the highest composition of pure tetragonal Zirconia [17]. At the outset, the comparative plot of thermal conductivities of common refractive oxides with respect to increasing temperature once again establishes a primary reason for the popularity of YSZ for the purpose of TBC.

TBCs, reportedly do not show substantial degradation in their properties over time while at service. Instead, they spall after a critical usage span, leading to catastrophic failure [18]. This failure is mainly attributed to thermo-mechanical fatigue along with chemical attack via CMAS (Calcium Magnesium Alumino Silicate) infiltration and erosive behaviour of the particulates encountered while being exposed to the aggressive environment of a gas turbine [19]. Therefore, difficulties persist in estimating a clear turnover point for replacing the coating.

As for the failure mechanisms, the most crucial among them is the one arising out of an uncontrolled variation in the thickness of the thermally grown oxide (TGO) layer formed between the TC and BC of the TBC due to the oxidation of the BC under operating conditions. The residual stresses caused by the oxidation of the BC are instrumental in affecting the life cycle of the TBC. The change in the crystallographic phase of the topcoat increases the crack density, initiates rumpling of the bond coat and leads to saturation in the growth of the oxide layer, indicative of the impending failure. It can be concluded that the appreciable ability of the BC and TC layers to prevent the increase in stress caused by mismatch in thermal expansion coefficient [20,21] is countered by the TGO occurring due to oxidation of the BC.

As discussed earlier, it is imperative to reiterate that the primary purpose of TBC to produce a significant resistance to the easy degradation of superalloys exposed to high-temperature applications. Failure through friction and wear are the most crucial concerns that pose a threat to the durability of the superalloys in such conditions. However, even the best TBCs fail to retain their wear-resistant characteristics for the prolonged application. Therefore, estimating the period determining the life of the YSZ-coated superalloys is pivotal in selecting for high-temperature applications under the influence of the prevalent failure conditions [22,23]. For this purpose, the wear test has proved to be the first choice for several research studies and industrial experimentation for predicting the approximate service life of TBCs under constant friction and wear attacks [24,25]. Hence, in this present study, an attempt has been made to track the history of wear and degradation of the TBCs through a comparative analysis of the coatings obtained after different intervals of degradation considering multiple modes of failure during the lifetime of the TBC with an aim towards obtaining a rough prediction of the remnant lifetime of the coatings.

2. Materials and methods

The samples used for the present investigation were sectioned from the interior of a functioning gas turbine. Three sets of samples were cut out using an electric discharge machining (EDM) device, as depicted in Fig. 2(a–c). One was obtained from a freshly coated and unexposed stock part, while the other two were cut from regions that had already been in use for 500 and 1000 service cycles. For the sake of convenience, a table representing the nomenclature of the sample types used throughout the manuscript has been provided in Table 1 for reference.

To prepare the samples for experimental investigations, the machined cross-sections were smoothened on emery paper with grit sizes ranging between 600 and 1200 (P1200–P4000), followed by cloth polishing using abrasive particles. Further, diamond polishing (1 μm) was performed on these edges to leave behind a mirror finish. The sample exposing the bare alloy (Fig. 3) surface was prepared similarly after grinding away the coating. It was further etched with the waterless Kalling's reagent (stock solution: 1 g Copper (II) Chloride, 20 ml HCl, 20 ml Ethanol) by swabbing technique. Some of these samples were cold-mounted using an epoxy resin for

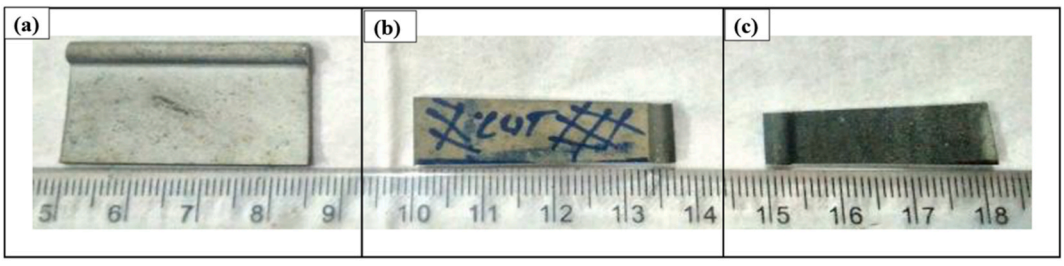

Fig. 2. A set of samples after EDM cutting (machined edge facing the scale, and TC facing the camera module) identified from the left as SN, S500 & S1000.

Table 1
Sample nomenclature and description.

Nomenclature of the sample	Description of the sample
SN	New – unused stock part
S500	In use for 500 service cycles
S1000	In use for 1000 service cycles

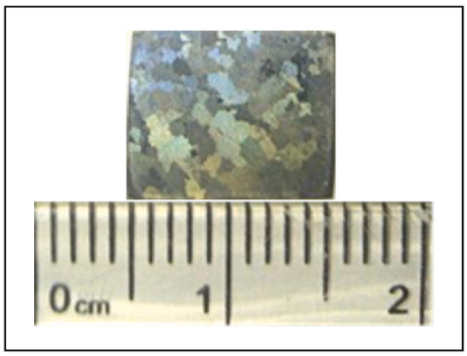

Fig. 3. Bare alloy after etching.

conducting optical microscopy and profilometry.

For the experimental investigations, the Inverted Metallurgical Optical Microscope (Carl Zeiss: Axio Observer Model) was trained on the samples at various magnification scales. Green light from an inbuilt LED was used to illuminate the sample. The three objective lenses were used successively for 5*X*, 10*X*, and 100× magnification, with the sample stage being adjusted accordingly to bring it close to the focal point. The aperture was controlled to limit it to the order of field of view in focus. The eyepiece featured a 10*X* magnifying lens and a CCD (AxioCamICc5) sensor, which provided a live display of the microstructure using the application suite.

Tribometry and wear tests were conducted on the coating to deduce the specific wear rate of the material used in the TBC, which is directly related to the fracture toughness of the coating since the fracture toughness depends on the hardness-to-elasticity ratio [26]. JEOL-made JSM-7610 F Schottky Field Emission-based Scanning Electron Microscope (SEM) was operated at 15 kV for source electrons along with a Silicon-Drift-Detector (X-MAX by Oxford Instruments) for Energy Dispersive Spectroscopy (EDS) to map the distribution of the elemental constituents. CAMECA made SX100 SEM primed at 20 KV, and its Electron Probe Micro-Analyzer (EPMA) proved invaluable during quantitative analysis for investigating the composition. The EPMA is a Wavelength Dispersed Spectrum Detector featuring four crystals identified as Thallium Acid Phthalate (TAP), Lithium Fluoride (LIF), Pentaerythritol (PET) and Large PET (LPET).

A Cobalt-anode-based X-Ray (narrow-band K-alpha-1) Powder Diffraction unit – Phillips PW 1830 was used in Bragg-Brentano mode. The $\boldsymbol{\theta}$-$\boldsymbol{\theta}$ goniometer was adjusted to scan an entire range of 20°–100° with steps of 12'. The XRD spectrum (Fig. 11) was corrected and matched with a known powder diffraction database (ICCD) available through HighScorePlus software.

The microhardness test was conducted using a digital microhardness tester (Leica) with a pyramidal diamond tip for the Vickers indentation method. The impression left on the region of interest is resolved using the built-in optical microscope for gauging the diagonal lengths. The hardness value in the HV index was automatically calculated from the input data and displayed.

A Bruker-made Contour GT model and Vision64 image analysis software achieved optical profilometry. The machine was operated in vertical scanning interferometry mode over a one mm^2 on each sample surface, which was then captured by the inbuilt image sensor. The noise threshold was set to 4% to validate a higher number of data points since the surface microstructure is supposed to be rough. This type of experiment for degradation test was conducted at room temperature (25 °C) "Ball on Disk" – wear Test. The tribometer used for this purpose was an automated Universal Micro Tribometer: UMT-2 manufactured by CET. Disk-shaped samples of 20 mm diameter and 1.5 mm thickness were prepared. A 6 mm diameter zirconia ball was used against the TC surface of the three samples at constant normal loads of 5, 10, 15, 20, and 25 N over radii 2, 4.5, 6, 7.5 and 9 mm tracks, respectively. The sliding rate was fixed at 5 mm/s for 41 revolutions on each sample. The main objective being – the measurement of the specific wear rate and subsequent inference of the degradation in coating strength from its variation across the three sample regimes.

3. Results and discussion

3.1. Microstructural characterization of samples

Optical micrography was opted for the preliminary analysis of the microstructural haracterization of the samples under present investigation as presented in Fig. 4(a–c). Careful observations revealed that the microstructure of the base alloy or metallic substrate is similar to René 100 (Inconel-100) alloy, which is further affirmed after verifying the composition using spectroscopic studies. The base

Nickel alloy matrix is austenitic, having been cast through slow cooling, has allowed the formation of large submillimeter-sized grains. γ' precipitates of nickel titanite-aluminide are also dispersed throughout the matrix. Smaller secondary austenitic precipitates cover the remaining zones between subsequent larger γ precipitates.

A detailed cross-sectional analysis revealed the three distinct regions of the TBC system of the sample, visible in Fig. 5. The top coat is observed to be mostly less than 20 μm, while the bond coat is slightly thicker, even extending to the order of 30 μm on few occasions. Meanwhile, the base metal alloy appears to be defocused underneath.

In order to conduct microstructural characterization of higher accuracy, Secondary Electron Micrography (SEM) images were obtained. These electron images revealed a visibly rough TC at 100× magnification. Fig. 6(b) shows the sample cross-section revealing the three distinct layers starting from the left:TC, BC and BA. The BA and its corresponding microstructure were resolved using compositional mode of the SEM with back scattered electrons, revealingd the secondary γ precipitates to form smeared cuboidal shapes (Fig. 6(d)). This corresponds to the expected behaviour of coatings obtained through APS contrary to those obtained through VD, which are usually expected to appear columnar in shape. Moreover, the image in Fig. 6(a) exposes the porous topography of the coating, which significantly diminishes the thermal conductivity in case of the APS coating, much in contrary to the observations of the base alloy in Fig. 6(c).

3.2. Chemical characterization

3.2.1. EDS

The spectroscopic maps of the cross-section were obtained to present an idea of the elemental distribution. The specimen chosen for this investigation was exposed for 1000 service cycles. The extreme left portion of the spectroscopy of Fig. 7(a and b) shows a coincidence of Zirconium, Yttrium, and Oxygen, which can be assumed to be the top coat of the sample. Considering that the topcoat is entirely composed of Yttrium (III) Oxide and Zirconium (IV) Oxide, the weight percentage of Yttria can be calculated to be 3.5. This indicates that the Zirconia present in the TC exhibits the tetragonal lattice type of crystal structure, which is in exact correspondence with the aim of YSZ coating [27].

The line data was obtained further to determine the thickness of the various layers. The layers are identified starting from the left. With Fig. 8(a) representing the point of inspection, due to the natural curvature of the sample, the EDS data is relevant to the sample counting from the 14 μm mark as depicted in Fig. 8(b). The TC ranges about 16 μm in thickness, similar to that of the BC, which appears to be chromate treated and 20 μm thick. The TGO layer has a thickness of less than 2 μm, and for this sample, it seems to have formed midway through the bond coat, possibly due to crevices left behind during deposition. This may have allowed the oxygen to seep deeper beyond the BC, forming the additional 3 μm thick protective alumina layer over the base alloy. From the above discussion, the micrographic characterizations obtained from the optical analysis, SEM imaging and EDS indicate to be in good agreement with each other.

3.2.2. Wavelength dispersive spectroscopy – WDS

The proper compositional distinction between the TBC layers was successfully obtained through the cross-section analysis of WDS represented in Fig. 9(a) along with Fig. 9(c) depicting a top view of the BA. The brightest layer on top is the TC of modified Zirconia, while the relatively greyer bond coat sits between the TC and the substrate. The darkest lines represent thermally grown oxides (TGO), a protective alumina coat at the bottom, and chromate at the interface of the TC and BC. The surface of the top coat is microstructurally slightly different from the bulk due to maximum thermal exposure at service and diffusion encountered, as is also suggested by Fig. 9 (b). Therefore, the image for the top coat indicates the inherent roughness by the plasma spraying process.

The WDS records (Fig. 10) revealed and supported the substrate to be René 100 (Inconel-100) Nickel Superalloy, the compositional distribution of which is presented in Table 2. The variation of the constituents is also in line with the different layers of the TBC system.

The weight percentage of Yttria in the top coat analyzed separately differs from that of the cross-section. This could be due to errors in point analysis introduced by erosion and subsequent contamination of the Zirconia (in that specific region, in the case of the cross-sectional analysis) during sample preparation, which made the signals from the contaminants wash over the X-Ray signal from the

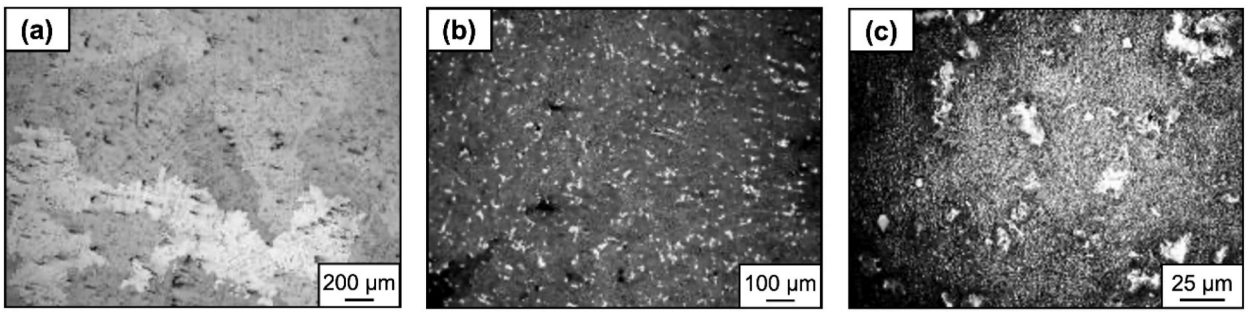

Fig. 4. Optical Micrographs of Base Alloys: (a) at 5× magnification highlighting grain boundaries using Kalling's waterless reagent (b) focused on a grain at 10*X* after etching with Aqua regia to reveal the γ' precipitates (c) the secondary γ precipitates at 100*X* after being etched with Keller's Reagent.

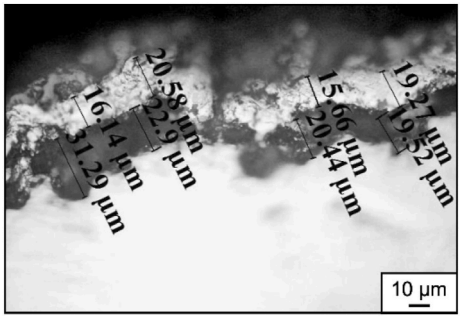

Fig. 5. Cross-sectional view at 50× magnification.

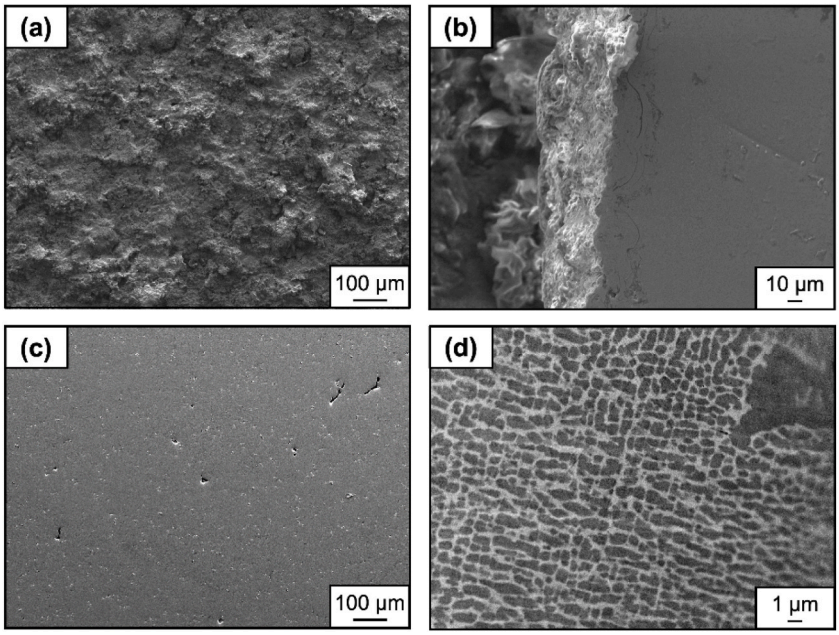

Fig. 6. Secondary Electron Image of the (a) top coat (b) sample Cross-section (c) secondary electron image of the base alloy (magnification: 100×) (d) composition mode - back scattered image (magnification: 3500*X*).

desired Yttria and Zirconia atoms. The separate analysis of the TC gives a result more concurrent with the EDS result, proving that a more reliable estimate is obtained in a non-local space.

3.2.3. X-Ray Diffraction

The diffraction spectrum for the SN and S500 display a similar peak profile, closely resembling the tetragonal phase of Zirconia (Fig. 11). To the contrary, the spectrum for Sample 1000 differs significantly because of damage encountered at service involving high-temperature exposure for prolonged periods. In due course, the tetragonal phase underwent stress induced phase transformation to monoclinic while cooling down.

The ratio of the corresponding phases can be collected from the intensity data. It revealed an expected increment in the monoclinic phase with the increase in the number of cycles experienced by the samples in working conditions. While for SN it is found to be in the order of 10%, in case of S500, it is 20% and over 60% in case of the S1000.

3.3. Micro-hardness

Three regions of interest (ROI) were selected on which the tests for the estimation of microhardness were conducted: On (i) the TBC layer and (ii) the substrate from the cross-sectional view, and (iii) on the TC surface normally. For the tests where the indenter was forced on the cross-sectional faces, the load was set at 100gf for a dwell time of 60s while it was increased to 500gf for 6s duration in the case of the normal face of the TC. It is difficult to focus on artefacts over the TC at high magnification because of its inherent roughness. 500gf was the optimum load value for not going beyond the estimated half point (5 µm) of the thickness of TC yet obtaining an

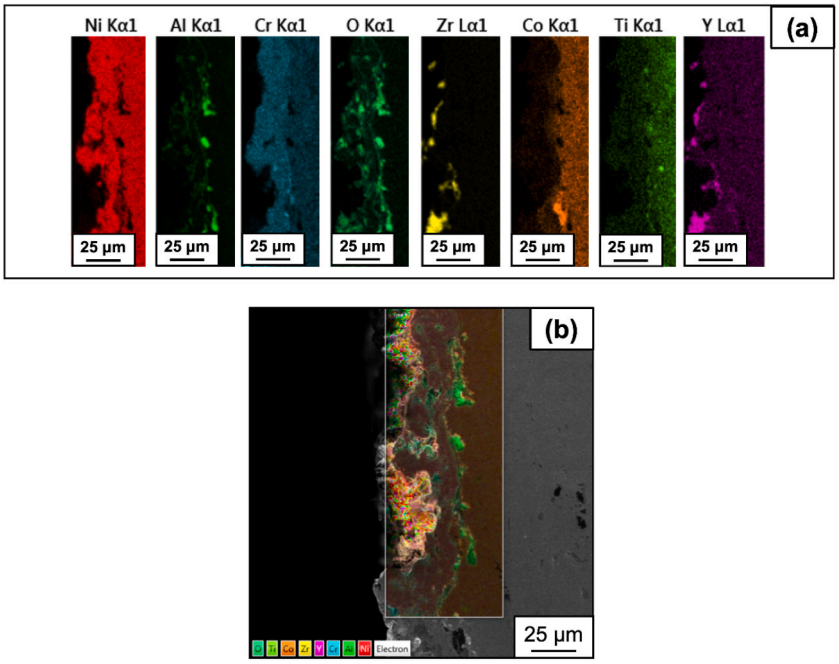

Fig. 7. EDS based Elemental Mapping of the Sample ID 1000 (Cross-section): (a) element wise segregated images (b) composite of all the Maps.

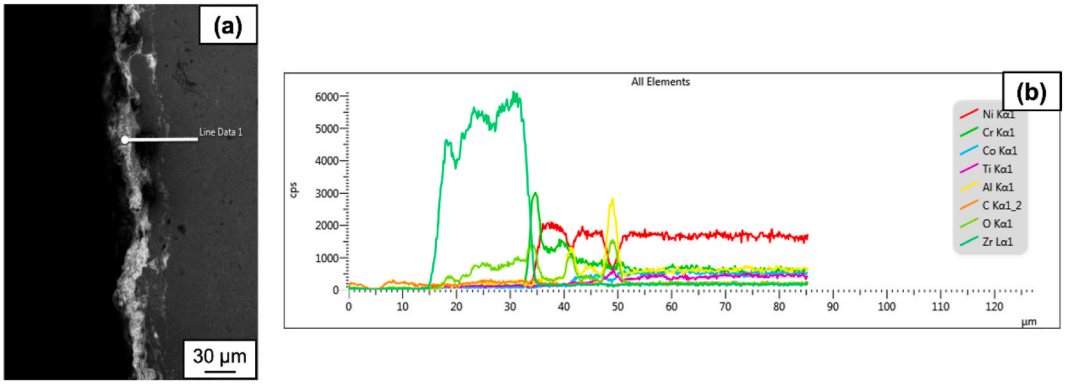

Fig. 8. (a) The segment whose line data was collected (b) EDS based intensity profile along the cross-section.

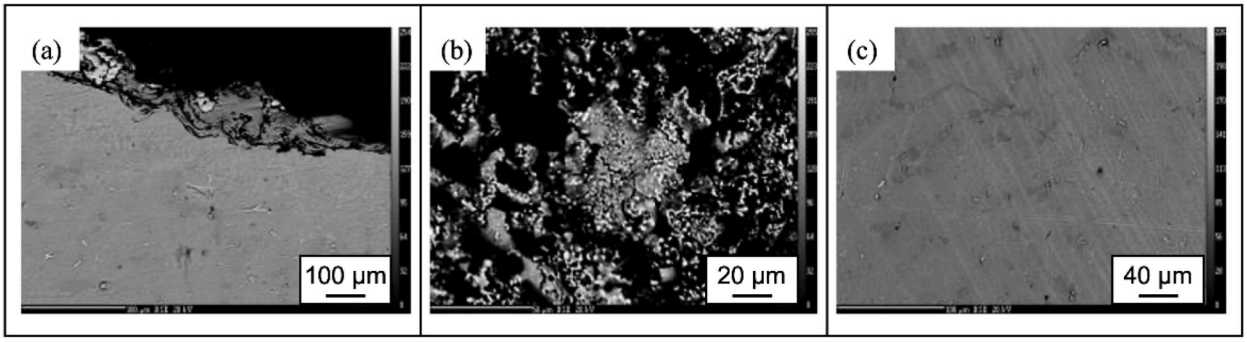

Fig. 9. Back Scattered Image of the corresponding portions whose WDS Spectra were collected (a) sample cross-section (b) top view of the rough TC (c) top view of the BA.

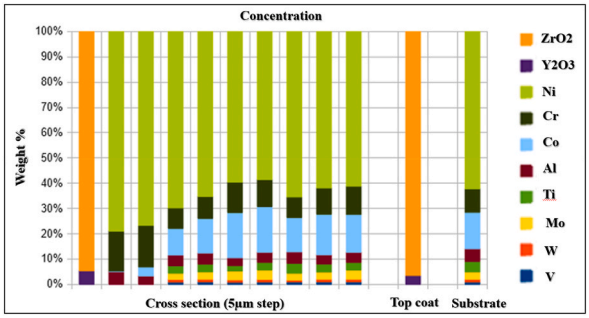

Fig. 10. Collective histogram of the varying elemental concentrations revealing the layers of the TBC.

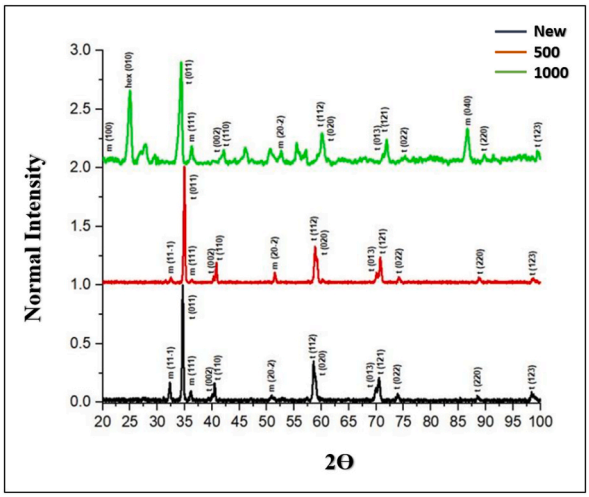

Fig. 11. XRD plot of X-ray counts with respect to twice the diffraction angle. The phase transformation from tetragonal to monoclinic bears evidence of the damage encountered by the samples with exposure to temperature, increasing with time.

Table 2
Compositional distribution of René 100.

Elements	Nickel	Cobalt	Chromium	Aluminum	Titanium	Molybdenum	Vanadium	Iron
Wt %	61	15	9.5	5.5	4.2	3.0	1.0	balance

impression (diagonal order ~ 30 μm) just about discernible under the microscope at lower magnification.

Similarly, 100gf was the minimum load was required to see an appreciable impression under the microscope, owing to the roughness of the cross-section of the system. Thus, the hardness profile of the TBC system could not be assessed (from the top) as its total thickness is comparable to the diagonal lengths (~23 μm). The surface hardness values of the alloy were determined (penetration depth <3 μm) as enumerated in Table 3.

The TBC hardness presented here signifies the adhesive strength of the system, which is necessary for successful implementation in high-temperature applications. The TC hardness order is close to those mentioned by certain manufacturers of YSZ, which ensures the proper layering of the thermal barrier coating on the top surface. Also the hardness of the substrate is in agreement with surface hardness values expected for René 100 (Inconel-100) [28]. This again supports the conclusions drawn from the microstructural and compositional characterisations similar to recent studies [29].

Table 3
Micro-hardness data.

R. O. I	H·V	Hardness (GPa)
TC (Normal)	965.3	9.467
TBC (Cross-section)	347.4	3.407
Substrate (Cross-Section)	463.8	4.548

3.4. Tribological characterization of the samples

3.4.1. Optical profilometry

Upon careful observation, the profilometry results revealed the artefacts of the TC as a pattern of dispersed red spots. Since the coating is porous, the roughness values are related to the thickness of the top coat. The average (R_a) and root mean squared (R_q) roughness values point toward the degradation of the TC at service, with the natural roughness (plasma spray) being lost with time. False colour micrographs have been generated from the roughness values with the red spots representing maximum roughness and blue spots – the least.

For each sample, the measurement having the highest indexation has been presented. Indexing has mostly been on the upper end of 90%, implying that the accuracy of the recorded data can be well accounted for. As will further be substantiated in the following tribological characterisations, the roughness data points to a trend of diminishing roughness (as we move from SN to S1000), the visual evidence of which can be linked with the dwindling population of red spots and a boost in the number of spots towards the blue end of the spectrum as represented in Fig. 12(a–c). This finding forms the basis of the prominent and expected observation that the spillage of the TBCs for the samples that have experienced more cycles of operation will be more probable.

3.4.2. Analysis of wear tracks

The wear tracks were resolved under an optical microscope and profilometry was conducted to reveal and measure their dimensions (Fig. 13). The track width and depth data were collected and averaged. For each sample, a pair of slices were profiled from its left and right halves (Fig. 15). As expected, the penetration depth and track width increased with load increment. These values also increase with the number of service cycles exposed to the sample. This brings the durability of the S1000 into question.

The images of the wear tracks Fig. 13(a–c) have been used to pass a qualitative judgement on the magnitude of the damage from the indenter footprints. With reference to the 150× magnified images presented in Fig. 14(a–c) it can be asserted that the wear mechanism initially involves plateauing the roughness in patches rather than scraping off the top coat, which became more pronounced for a higher number of laps. The number of such damaged sites, their area and spread increase over the range of the three samples, leading to higher depth and greater width of the tracks.

A better picture of wear analysis can be obtained by evaluating the specific wear rate of the material [30]. The specific wear rate (SWR) is directly related to the worn-out volume and is calculated by Archard's Model:

$$\textbf{SWR}\ (\mathrm{mm^3/Nm}) = \{\textbf{Wear Volume}\ (\mathrm{mm^3})\}\ /\ [\{\textbf{Sliding Distance}\ (\mathrm{m})\}\ *\ \{\textbf{Load}\ (\mathrm{N})\}] \quad (1)$$

While the wear profiles used for the SWR calculations can be referred from Fig. 15(a–c), the wear volume was estimated by evaluating the cross-sectional area of the track slices and multiplying it by track circumference, while the sliding distance and loads were known beforehand. Fig. 16 (a) represents the SWR w.r.t. The applied load for each sample to clearly visualize the influence of service life on the wear behaviour. Further, Fig. 16(b) reveals that the wear resistance decreases gradually with the number of service cycles exposed and the decline in its magnitude was more significant for the loading range 10N–20 N. It was noted that around 25 N the wear rates for all the three samples were of an equivalent order of magnitude. At the same time, SWR of the S1000 saturated around 0.007 $\mathrm{mm^3/N\text{-}m}$, signifying that value to be the limiting neighborhood for samples with tetragonal structure.

3.4.3. Coefficient of friction (μ)

The coefficients of dynamic friction were evaluated for every sample from the PID sensor data collected on the effective normal reaction force and the tangential undertow experienced by the ball. Since the roughness values follow a decreasing mode (evident from section 3.4.1), the dynamic coefficient of friction values is also expected to reveal similar behaviour. Simply put, the resistance experienced by the ball decreases correspondingly with an increase in a number of cycles of operations for the samples. This finding is entirely in agreement with the observation of surface profilometry study.

Fig. 17 represents the μ values for different samples and conditions. The anomaly found in case of 5 N load for S1000 can be attributed to the incorporation of various sources of errors such as sample surface contamination, discrepancies introduced by virtue of sample preparation or human errors while conducting the experimentations. With careful investigation, it can be concluded that the error percentage in this anomaly is absolutely insignificant in comparison to the magnitude of the results. Moreover, most of the results, including optical, chemical and tribological characterisations, point to the fact that reliability of the experimental outcomes in the present study should not be questioned. The clear agreement among all the results and the assumptions of the present study indicates the accuracy of the tests conducted.

3.4.4. Wear resistance (WR)

Most researchers quantify WR with a number inversely proportional to the SWR. Herein the WR of the samples have been user defined as:

$$WR = \frac{\frac{1}{\text{Specific Wear Rate}}}{\frac{1}{\text{Specific Wear Rate NEW @ 5N}}}\ \text{X}\ 100$$

The plot shown in Fig. 16(b) displays the variation of WR with the number of cycles that the sample has been exposed to. Irrespective of the loading range 10–25 N, the values clump around the 3–4% demarcation for the WR with respect to the freshly coated sample. This may indicate that the coating will only be durable when the operation variables are modified to more suitable conditions.

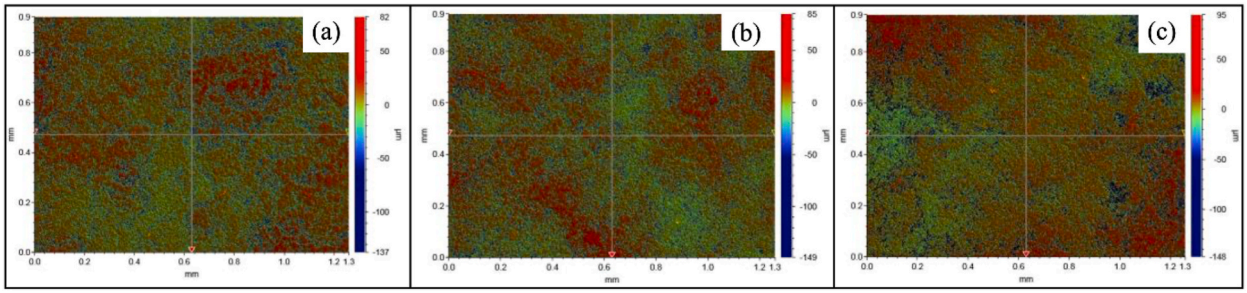

Fig. 12. False colour micrograph of sample (a) SN (b) S500 (c) S1000

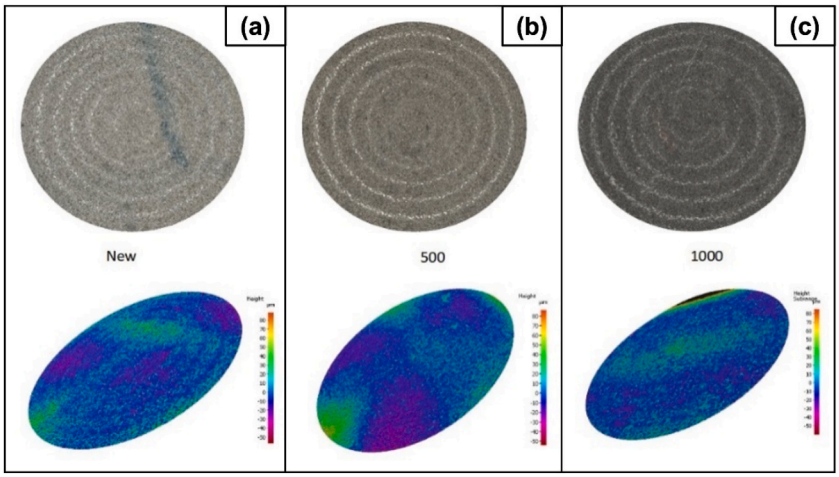

Fig. 13. Images of wear tracks on the samples (a) SN (b) S500 (c) S1000.

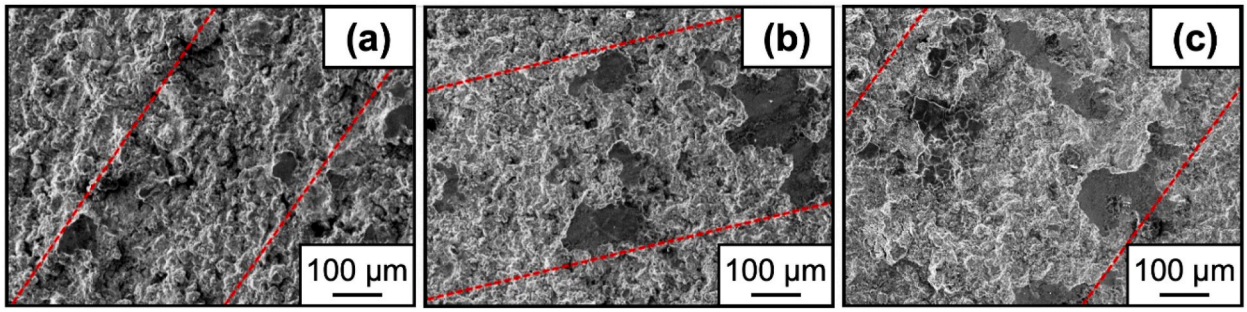

Fig. 14. SEM images of the tracks on each sample, for 20 N load for samples (a) SN (b) S500 (c) S1000.

With this, it can be concluded that the S500 and S1000 samples showed significant deterioration in wear-resisting ability compared to the unused SN samples. Furthermore, the decrease a significant decrease in the coefficient of friction values as we gradually shift from SN to S1000, indicates the heavy influence of operating time on the durability of the coatings. Therefore, tribometry tests justify that the coating has severely degraded after 1000 cycles; hence, the part of the superalloy would need to be re-coated.

4. Conclusion

The primary intention of this study was to establish an accurate relationship between the results obtained from the tribological investigations with the estimated period of service of the YSZ coatings. Optical profilometry, wear resistance ability, specific wear rate and the trend in values for the coefficient of friction as we gradually moved from SN to S500 and finally to S1000, successfully revealed a precise estimation of the maximum period of durability for the TBCs. Apart from the conclusions of the tribometry tests, the present study also provided a perfect agreement amongst the various results in several compositional and microstructural characterizations.

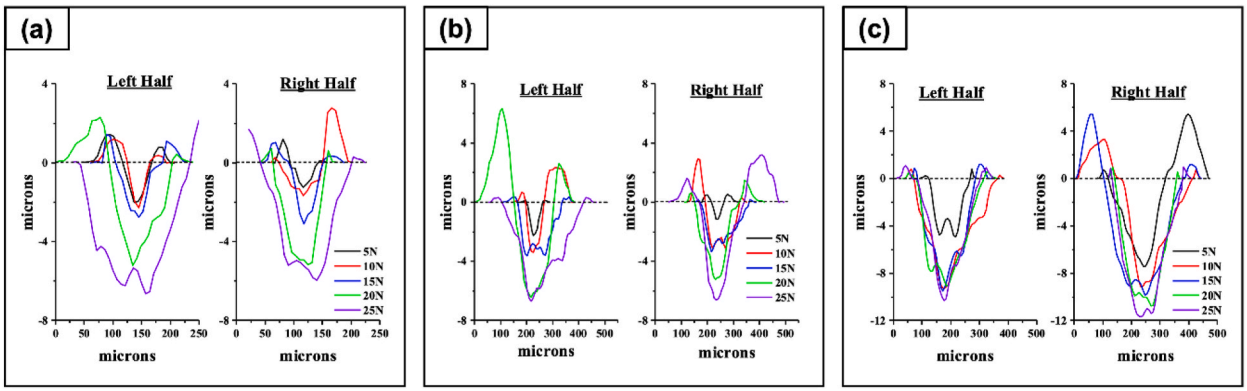

Fig. 15. Wear profiles for calculating SWR (a) SN (b) S500 (c) S1000.

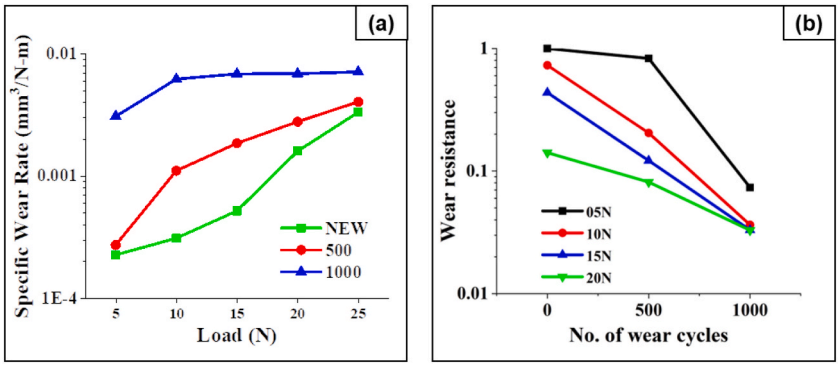

Fig. 16. (a) SWR of the three samples across a range of loading conditions (b) Wear resistance vs number of cycles.

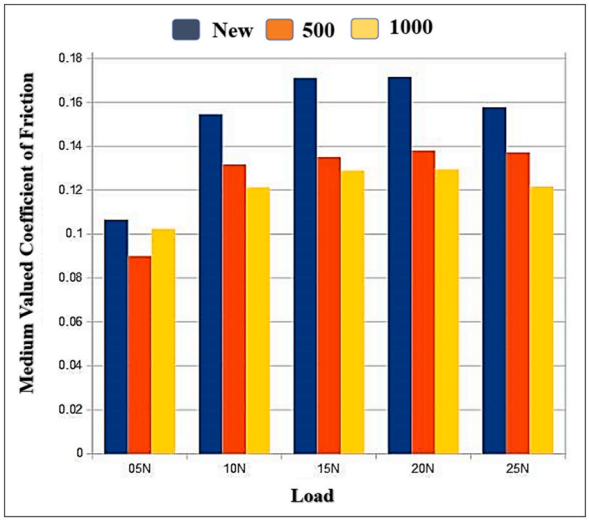

Fig. 17. A trend in values of μ decreasing gradually for SN, S500 and S1000.

The TBC system was verified to be: YSZ top coat and (Ni/Co)CrAlY bond coat while optical, EDS and WDS revealed the base alloy substrate to be René 100 superalloy with the presence of γ' precipitates of nickel titanite-aluminide. The optimized concentration for the Ytrrium doping to minimize stress-induced transformation of Zirconia was obtained to be about 3.5 wt %. The top coat is around 10–20 μm thick while the thickness of the bond coat is of slightly higher magnitude with a different TGO layer. Besides the expected layers of a conventional TBC, additional protective oxide layers of Chromium and Aluminium were also detected over the BC and the

BA respectively, through EDS and WDS analysis. Spectroscopic image analysis also reveals the cause of adhesion among the binding of the layers to be inner diffusion. YSZ TC was mainly concluded to be in the tetragonal phase for the SN. The stress-induced transformation from the tetragonal to monoclinic phase was noticeably visible from the XRD data analysis of SN, S500, and S1000 which points towards the underlying deterioration of fracture toughness or wear resistance values. Lastly, the average and root mean square linear roughness depreciation from SN to S1000 corresponds to erosion. The wear resistance of the S1000 was the lowest with its wear durability predictably much higher than the rest.

While the reliability and accuracy of the present study is proved from the good agreement of the results among themselves, there are a few future scopes open for further investigations for enhancing the quality of the results obtained. Some of them can be the characterization of the exposed alloy by 3D profilometry for surface roughness values (S_a) and rumpling wavelength. Additionally, one can look into high-temperature thermal conductivity by using laser-assisted infrared thermometers which can be targeted on the backside of the thin samples while a blowtorch is used to scorch the top coat surface. The thermal conductivity of the base alloy and inter-metallic bond-coat can also be evaluated separately in bulk for results of higher accuracy.

Author contribution statement

Pushpak Banerjee: Conceived and designed the experiments; Performed the experiments; Analyzed and interpreted the data; Wrote the paper.

Avinava Roy, Soumyadeep Sen: Analyzed and interpreted the data; Wrote the paper.

Arkajit Ghosh, Gourab Saha: Analyzed and interpreted the data.

Asiful H. Seikh, Ibrahim A. Alnaser: Contributed reagents, materials, analysis tools or data.

Manojit Ghosh: Conceived and designed the experiments; Analyzed and interpreted the data; Contributed reagents, materials, analysis tools or data.

Data availability statement

Data will be made available on request.

Funding statement

This research was funded by the Researchers Supporting Project number RSPD2023R597.

Declaration of competing interest

The authors declare that they have no known competing financial interests or personal relationships that could have appeared to influence the work reported in this paper

Acknowledgements

The authors would like to acknowledge the Researchers Supporting Project number (RSPD2023R597), King Saud University, Riyadh, Saudi Arabia.

References

[1] E. Çelik, İ.A. Şengil, E. Avcı, Effects of some parameters on corrosion behaviour of plasma-sprayed coatings, Surf. Coating. Technol. 97 (1–3) (1997) 355–360, https://doi.org/10.1016/S0257-8972(97)00208-9.

[2] L.B. Chen, YTTRIA-STABILIZED zirconia thermal barrier coatings — a review, Surf. Rev. Lett. 13 (5) (2006) 535–544, https://doi.org/10.1142/S0218625X06008670.

[3] E.H. Kisi, C.J. Howard, Crystal structures of zirconia phases and their inter-relation, Key Eng. Mater. 153–154 (1998) 1–36. https://dx.doi.org/10.4028/www.scientific.net/KEM.153-154.1.

[4] H.M. Choi, B.S. Kang, W.K. Choi, D.G. Choi, S.K. Choi, J.C. Kim, Y.K. Park, G.M. Kim, Effect of the thickness of plasma-sprayed coating on bond strength and thermal fatigue characteristics, J. Mater. Sci. 33 (24) (1998) 5895–5899, https://doi.org/10.1023/A:1004439123350.

[5] R. Westergard, L.C. Erickson, N. Axen, H.M. Hawthorne, S. Hogmark, The erosion and abrasion characteristics of alumina coatings plasma sprayed under different spraying conditions, Tribol. Int. 31 (5) (1998) 271–279, https://doi.org/10.1016/S0301-679X(98)00033-4.

[6] J. Matejicek, S. Sampath, Intrinsic residual stresses in single splats produced by thermal spray processes, Acta Mater. 49 (11) (2001) 1993–1999, https://doi.org/10.1016/S1359-6454(01)00099-4.

[7] S. Ghosh, Thermal barrier ceramic coatings — a review, in: Advanced Ceramic Processing, InTech, 2015, https://doi.org/10.5772/61346.

[8] W.D. Kingery, H.K. Bowen, D.R. Uhlmann, Introduction to Ceramics, second ed., Wiley, 1976.

[9] D.G. Cahill, P.v. Braun, G. Chen, D.R. Clarke, S. Fan, K.E. Goodson, P. Keblinski, W.P. King, G.D. Mahan, A. Majumdar, H.J. Maris, S.R. Phillpot, E. Pop, L. Shi, Nanoscale thermal transport. II. 2003–2012, Appl. Phys. Rev. 1 (1) (2014), 011305, https://doi.org/10.1063/1.4832615.

[10] Abdullah Cahit, et al., Thermal shock and cycling behavior of thermal barrier coatings (TBCs) used in gas turbines, in: Progress in Gas Turbine Performance, InTech, Crossref, 2013, https://doi.org/10.5772/54412.

[11] R. Vaben, M.O. Jarligo, T. Steinke, D.E. Mack, D. Stover, Overview on advanced thermal barrier coatings, Surf. Coating. Technol. 205 (4) (2010) 938–942.

[12] Z.Y. Wei, G.H. Meng, L. Chen, G.R. Li, M.J. Liu, W.X. Zhang, C.J. Li, Progress in ceramic materials and structure design toward advanced thermal barrier coatings, J. Adv. Ceram. 11 (7) (2022) 985–1068.

[13] Y. Guo, W. Song, L. Guo, X. Li, W. He, X. Yan, H. Guo, Molten-Volcanic-Ash-Phobic Thermal Barrier Coating Based on Biomimetic Structure, Advanced Science, 2023, 2205156.

[14] R.H.J. Hannink, P.M. Kelly, B.C. Muddle, Transformation toughening in zirconia-containing ceramics, J. Am. Ceram. Soc. 83 (3) (2004) 461–487, https://doi.org/10.1111/j.1151-2916.2000.tb01221.x.
[15] S. Stecura, Optimization of the Nicral-Y/Zro-Y2o3 Thermal Barrier System, Meeting of the American Ceramic Society, Ann, 1985.
[16] E. Bakan, R. Vaben, Ceramic top coats of plasma-sprayed thermal barrier coatings: materials, processes, and properties, J. Therm. Spray Technol. 26 (2017) 992–1010.
[17] Z.-G. Liu, J.-H. Ouyang, Y. Zhou, J. Li, X.-L. Xia, Influence of ytterbium- and samarium-oxides codoping on structure and thermal conductivity of zirconate ceramics, J. Eur. Ceram. Soc. 29 (4) (2009) 647–652, https://doi.org/10.1016/j.jeurceramsoc.2008.07.033.
[18] D.R. Clarke, S.R. Phillpot, Thermal barrier coating materials, Mater. Today 8 (6) (2005) 22–29, https://doi.org/10.1016/S1369-7021(05)70934-2.
[19] S.T. Aruna, N. Balaji, K.S. Rajam, Phase transformation and wear studies of plasma sprayed Yttria stabilized zirconia coatings containing various mol% of Yttria, Mater. Char. 62 (7) (2011) 697–705, https://doi.org/10.1016/j.matchar.2011.04.018.
[20] Coatings for High-Temperature Structural Materials, National Academies Press, 1996, https://doi.org/10.17226/5038.
[21] R.B. Thompson, L.J.H. Brasche, Nondestructive evaluation, in: Turbine Aerodynamics, Heat Transfer, Materials, and Mechanics, American Institute of Aeronautics and Astronautics, Inc, 2014, pp. 555–583, https://doi.org/10.2514/5.9781624102660.0555.0584.
[22] M. Caliez, F. Feyel, S. Kruch, J.-L. Chaboche, Oxidation induced stress fields in an EB-PVD thermal barrier coating, Surf. Coating. Technol. 157 (2–3) (2002) 103–110, https://doi.org/10.1016/S0257-8972(02)00167-6.
[23] K.W. Schlichting, N.P. Padture, E.H. Jordan, M. Gell, Failure modes in plasma-sprayed thermal barrier coatings, Mater. Sci. Eng., A 342 (1–2) (2003) 120–130, https://doi.org/10.1016/S0921-5093(02)00251-4.
[24] J.D. Frieman, H. Kamhawi, G.J. Williams, W. Huang, D.A. Herman, P.Y. Peterson, J.H. Gilland, R.R. Hofer, Long duration wear test of the nasa hermes Hall thruster, in: AIAA, SAE and ASEE Joint Propulsion Conference, 2018.
[25] S. Sudhagar, V. Mugesh Raja, S. Sathees Kumar, A. Jonathan Samuel, The wear behavior and service life of Madar and Bauhinia Racemosa reinforced polyester hybrid composites for gear applications, Mater. Today: Proc. 19 (2019) 589–593, https://doi.org/10.1016/j.matpr.2019.07.738.
[26] G.R. Anstis, P. Chantikul, B.R. Lawn, D.B. Marshall, A critical evaluation of indentation techniques for measuring fracture toughness: I, direct crack measurements, J. Am. Ceram. Soc. 64 (9) (1981) 533–538, https://doi.org/10.1111/j.1151-2916.1981.tb10320.x.
[27] T. Gotsch, W. Wallisch, M. Stoger-Pollach, B. Klotzer, S. Penner, From Zirconia to yttria: sampling the YSZ phase diagram using sputter-deposited thin films, AIP Adv. 6 (2) (2016), 025119, https://doi.org/10.1063/1.4942818.
[28] R.S. Lima, Porous APS YSZ TBC manufactured at high powder feed rate (100 g/min) and deposition efficiency (70%): microstructure, bond strength and thermal gradients, J. Therm. Spray Technol. 31 (3) (2022) 396–414, https://doi.org/10.1007/s11666-021-01302-y.
[29] Y.M. Arisoy, C. Guo, B. Kaftanoglu, T. Ozel, Investigations on microstructural changes in machining of Inconel 100 alloy using face turning experiments and 3D finite element simulations, Int. J. Mech. Sci. 107 (2016) 80–92, https://doi.org/10.1016/j.ijmecsci.2016.01.009.
[30] M. Kadivar, B. Azarhoushang, Kinematics and material removal mechanisms of loose abrasive machining, in: Tribology and Fundamentals of Abrasive Machining Processes, Elsevier, 2022, pp. 507–536, https://doi.org/10.1016/B978-0-12-823777-9.00007-0.